NUMERICAL INVESTIGATION OF TURBULENT FLUID FLOW AND HEAT TRANSFER CHARACTERISTICS IN A STREAMWISE-PERIODIC CORRUGATED DUCT WITH CONSTANT CROSS-SECTIONAL AREA

BIJAN FARHANIEH AND BENGT SUNDEN

Department of Thermo- and Fluid Dynamics, Chalmers University of Technology, S-412 96 Göteborg, Sweden

ABSTRACT

Turbulent fully developed periodic heat transfer and fluid flow characteristics in corrugated two-dimensional ducts with constant cross-sectional area are numerically investigated. The governing equations are solved numerically by a finite-volume method for elliptic flows in complex geometries using collocated variables and Cartesian velocity components. Two different turbulence models (the second moment closure and the $k-\varepsilon$) for approximation of the Reynolds stresses are applied. The performance of the models were assessed by comparing the results with experimental data. The results show the advantages of the stress closure model compared to the $k-\varepsilon$ model. The overall Nusselt number and the pressure drop ratio results are obtained for the boundary condition of a uniform wall temperature for two inclination angles ϕ and two duct aspect ratios (H/L) and for Reynolds number ranging from around 3000 to 35,000. The overall Nusselt number predicted by the $k-\varepsilon$ model is upto 25% higher than the values predicted by the second moment closure. The plots of the velocity vectors show a complex flow pattern. The mechanisms of heat transfer are explained by the flow phenomena separation, deflection, recirculation, and reattachment.

KEY WORDS   Corrugated ducts   Turbulent fluid flow   Finite volume method

NOMENCLATURE

A	per-cycle heat transfer surface area
c_p	specific heat
D_h	hydraulic diameter ($= 2H$)
f	wall-distance function
f_f	friction factor
G	scale factor of the velocity vectors
H	height of the duct
H^+	$U_* H/v$
h	heat transfer coefficient
h_{av}	average heat transfer coefficient
k	turbulent kinetic energy
k_c	thermal conductivity of the fluid
L	streamwise length of a module
$\dot{m}$	mass flow rate
n	normal vector

Nu	average Nusselt number
Nu_x	circumferential local Nusselt number
p	fluctuation pressure
P	pressure
P^*	periodic pressure
Pr	Prandtl number
$\dot{Q}$	per-cycle wall heat transfer rate
q_w	heat transfer rate at the well (per unit area)
Re	Reynolds number
S	top length of the cavity
S_Φ	source term in general equation
T	temperature
t	tangential vector
T^+	dimensionless temperature (39)
T_b	bulk temperature
T_{b1}	bulk temperature at the inlet of the module
T_{b2}	bulk temperature at the outlet of the module
T_b^+	dimensionless bulk temperature (57)
U	axial velocity
u	fluctuation velocity in main flow direction
U_i	velocity components
U_m	mean velocity
U_*	friction velocity
U_+	U/U_*
V	velocity in y-direction
v	fluctuation velocity in y-direction
x	streamwise coordinate
y	coordinate
y^+	$\rho U_* y/\mu$
β	non-periodic pressure gradient
Γ	turbulent diffusivity of heat
γ	bulk-to-wall temperature ratio
δ_{ij}	Kronecker delta
Δp	per-cycle pressure drop in corrugated duct
Δp_0	pressure drop in parallel plate duct
ΔT_{wb}	average wall-to-bulk temperature difference
ε	dissipation rate of the turbulent kinetic energy
η	distance normal to the wall
Θ	dimensionless temperature
λ	bulk-temperature-gradient parameter
μ	dynamic viscosity
v	kinematic viscosity
v_t	turbulent viscosity
ρ	density
$-\rho\overline{u_i u_j}$	Reynolds stress components
σ_t	turbulent Prandtl number or Schmidt number
σ_k	empirical diffusion constant ($= 1$)
σ_ε	empirical diffusion constant ($= 1.185$)
ϕ	corrugation angle

INTRODUCTION

Compact and efficient surfaces are attempted for in heat exchangers to reduce the heat exchanger costs. One way of achieving this is to employ wall-corrugated ducts in heat exchanger apparatus.

While there are many reports on studies of heat exchangers only few reports are focusing on the investigation of heat and fluid flow in corrugated ducts[1-5]. Three of these studies[1-3] are basically concentrated on experimental investigation of the ducts. O'Brien and Sparrow[1], and Izumi et al.[2] measured heat transfer rates in a corrugated wall channel with 120° and 90° bend angle, while Goldstein and Sparrow[3] investigated local mass transfer rates by means of naphthalene sublimation technique. O'Brien and Sparrow measured heat transfer rates for several different Pr with a fixed corrugation geometry, whereas Izumi et al.[2] adopted the corrugation period as a parameter while holding the fluid properties constant.

Farhanieh and Sundén[4] studied numerically the fully developed laminar fluid flow and heat transfer in a periodically corrugated wall duct. Corrugation angles of 45° and 15° with three different height to length ratios were considered. Amano et al.[5] studied numerically laminar and turbulent heat transfer in a periodically corrugated wall channel with 90° bend angle with and without fins. Faas and McEligot[6] have also studied laminar flows for channels with 90° bends.

There are some further numerical and experimental results available in the literature[7]. The numerical approach for solution of such geometries is based upon the assumption that the duct is long and consists of many identical modules in the streamwise direction where the fully developed velocity field repeats itself in a cyclic manner. This assumption enables us to ignore the influence of the entrance and exit regions and confine the calculation domain to cover only one of the modules.

The methodology for fully developed solutions of this kind of problem was presented by Patankar et al.[8] This methodology has been used by Sparrow and Prata[9,10] to study laminar flow and heat transfer in a periodically converging–diverging tube and in an annulus of periodically varying cross-section. Rowley and Patankar[11] applied this method in their study of tubes with internal circumferential fins. Faghri and Asako[12,13], Webb and Ramadhyani[14], Sundén and Trollheden[15], and Farhanieh and Sundén[16] have also successfully adopted this method in their studies of various ducts with streamwise-periodic variations of cross-sectional areas. Through these studies it has been shown that higher convective heat transfer coefficients can be achieved by employment of corrugated channels but the pressure drop is also increased.

In this work a finite-volume method for elliptic flows in non-orthogonal coordinates is applied. It utilizes collocated variables and Cartesian velocity components. The general details of the method are documented in a report by Davidson and Farhanieh[12] and have also been presented in a previous paper by Farhanieh and Sundén[13]. The Reynolds kinematic stresses $\overline{u_i u_j}$ are evaluated by full Reynolds-stress transport equations. However, the results are compared with those obtained by approximating the stresses by means of the Boussinesq eddy viscosity model.

Numerical solutions were carried out for a uniform wall temperature boundary condition at two values of the corrugation angle ϕ, and two values of the cycle aspect ratio ($= H/L$). The computations were performed in the Reynolds number (based on hydraulic diameter) range 3000 to 35,000 and for $Pr = 0.72$ corresponding to air. Nusselt numbers and pressure drop data as well as, velocity vectors are presented.

In an earlier paper by Farhanieh and Sundén[4], a similar study for laminar flow has been carried out.

PROBLEM FORMULATION

The duct considered is presented schematically in *Figure 1*. The oblique walls are positioned at an angle ϕ to the main flow direction. The geometry of the channel can be specified by the
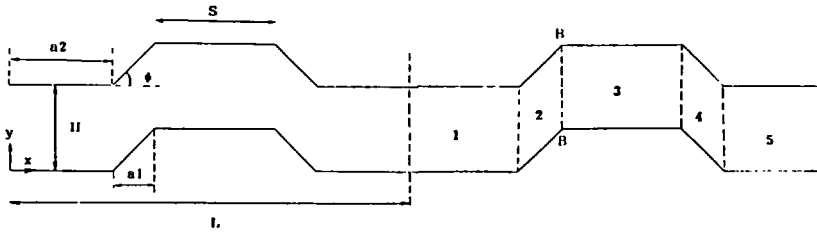
Figure 1 Schematic diagram of the duct

periodic axial full length L, the height H, lengths a_1, a_2 and S, and corrugation angle ϕ. The dimensions of the duct are: $a_1 = 0.1L$, $a_2 = 0.25L$ and $S = 0.3L$. The values of 15° and 45° were chosen for the corrugation angle ϕ. The ratio H/L is varied.

The heat transfer and fluid flow characteristics for turbulent, incompressible, forced convection along the cycle length are to be determined. The walls of the duct are kept at a uniform temperature. The axial velocity is in the x-direction.

GOVERNING EQUATIONS

The governing equations are the continuity, momentum and energy equations. Consideration is given to fully developed periodic turbulent flow. The flow is studied under the following assumptions: steady state, constant fluid properties, negligible viscous dissipation and no natural convection.

The pressure P, is expressed by:

$$P(x, y) = -\beta x + P^*(x, y) \tag{1}$$

where P^* behaves in a periodic manner from cycle to cycle. In βx, β is a constant representing the non-periodic pressure gradient in the flow direction.

The governing equations in Cartesian coordinates system read:

$$\frac{\partial U}{\partial x} + \frac{\partial V}{\partial y} = 0 \tag{2}$$

$$U\frac{\partial U}{\partial x} + V\frac{\partial U}{\partial y} = -\frac{\partial P^*}{\partial x} + \beta + v\left(\frac{\partial^2 U}{\partial x^2} + \frac{\partial^2 U}{\partial y^2}\right) + \frac{\partial}{\partial x}(-\overline{u^2}) + \frac{\partial}{\partial y}(-\overline{uv}) \tag{3}$$

$$U\frac{\partial V}{\partial x} + V\frac{\partial V}{\partial y} = -\frac{\partial P^*}{\partial y} + v\left(\frac{\partial^2 V}{\partial x^2} + \frac{\partial^2 V}{\partial y^2}\right) + \frac{\partial}{\partial x}(-\overline{uv}) + \frac{\partial}{\partial y}(-\overline{v^2}) \tag{4}$$

$$U\frac{\partial \Theta}{\partial x} + V\frac{\partial \Theta}{\partial y} - \frac{\partial}{\partial x}\left(\Gamma\frac{\partial \Theta}{\partial x}\right) - \frac{\partial}{\partial y}\left(\Gamma\frac{\partial \Theta}{\partial y}\right) = \sigma \tag{5}$$

where

$$\sigma = \lambda\left(\Gamma\frac{\partial \Theta}{\partial x} + \frac{\partial}{\partial x}(\Gamma\Theta) - U\Theta\right) + \Gamma\Theta\left(\lambda^2 + \frac{\partial \lambda}{\partial x}\right) \tag{6}$$

and

$$\lambda = \frac{\partial(T_b - T_w)}{\partial x}\bigg/(T_b - T_w) \tag{7}$$

where σ and λ are periodic parameters for the case of a constant wall temperature and T_b the fluid bulk temperature. The exchange coefficient Γ is defined as:

$$\Gamma = \frac{v}{Pr} + \frac{v_t}{\sigma_t} \tag{8}$$

where σ_t is the turbulent Prandtl number. The dimensionless temperature Θ is defined as:

$$\Theta = \frac{T - T_w}{T_b - T_w} \tag{9}$$

The velocity–temperature scalar fluctuation correlation which determines the turbulence diffusive flux $(\overline{-u_i\theta})$ is replaced by the Boussinesq viscosity approximation. The second moment closure has not been used for the temperature equation because the transport model for $(\overline{u_i\theta})$ is not well defined for the complex recirculating flows[5]. The turbulent kinematic viscosity v_t is calculated by $c_\mu k^2/\varepsilon$, where k is the turbulent kinetic energy, ε is the dissipation rate of the turbulent kinetic energy and c_μ is a constant (see below).

The shape of the non-dimensional temperature profile $\Theta(x, y)$ repeats itself in the fully developed periodic area.

Since the convective heat transfer equation contains two unknowns, $\Theta(x, y)$ and $\lambda(x)$, an additional condition is needed to close the problem. The dimensionless temperature Θ must be compatible with the definition of the bulk temperature. In dimensionless form we have:

$$\int \Theta |U| \, dA' = \int |U| \, dA' \tag{10}$$

This equation gives the lacking condition for the dimensionless temperature field.

Turbulence model

In the present work, turbulence is described either by the high Reynolds number k–ε eddy-viscosity model or by high Reynolds number Reynolds stress closure.

The first closure variant employed is the Boussinesq viscosity model[17] for approximating the stresses. In this method the turbulent stresses are assumed to be proportional to the mean rate of strain by analogy with the viscous stresses in laminar flow, i.e.

$$\rho\overline{u_iu_j} = -\mu_t\left(\frac{\partial U_i}{\partial x_j} + \frac{\partial U_j}{\partial x_i}\right) + \frac{2}{3}\delta_{ij}\rho k \tag{11}$$

The second closure variant adopted is that of Gibson and Launder[18]. The full Reynolds stress transport equations are solved for evaluations of the stresses.

$$(\rho U_k\overline{u_iu_j})_{,k} = D_{ij} + P_{ij} - \rho\varepsilon_{ij} + \Pi_{ij} \tag{12}$$

where the terms on the right hand side represent:

P_{ij}: the production rate of $\overline{u_iu_j}$:

$$P_{ij} = -\rho\overline{u_iu_l}U_{j,l} - \rho\overline{u_ju_l}U_{i,l} \tag{13}$$

ε_{ij}: the dissipation term of $\overline{u_iu_j}$:

$$\varepsilon_{ij} = 2v\overline{u_{i,l}u_{j,l}} \tag{14}$$

D_{ij}: the turbulent diffusion:

$$D_{ij} = -\rho\left(\overline{u_i u_j u_l} + \frac{\overline{pu_i}}{\rho}\delta_{jl} + \frac{\overline{pu_j}}{\rho}\delta_{il} \right)_{,l}$$ (15)

Π_{ij}: the pressure–strain correlation term which promotes isotropy of turbulence:

$$\Pi_{ij} = \overline{p(u_{i,j} + u_{j,i})}$$ (16)

In order to eliminate the unknown correlations appearing in the Reynolds transport equation, the pressure–strain, dissipation, and turbulent diffusion terms require model approximation.

The assumption of local isotropy enables us to approximate the dissipation of $\overline{u_i u_j}$ by:

$$\varepsilon_{ij} = \tfrac{2}{3}\delta_{ij}\varepsilon$$ (17)

where ε is the dissipation rate of the turbulent kinetic energy.

The fluctuating pressure p can be eliminated from the pressure–strain correlation via a Poisson equation for p. It can be shown that there are three distinct processes which contribute to the pressure–strain correlation:

1. Interaction of fluctuating velocities $(\Pi_{ij})_1$ which is also referred to as return-to-isotropy term[19]:

$$(\Pi_{ij})_1 = -\frac{\rho c_1 \varepsilon}{k}\left(\overline{u_i u_j} - \frac{\delta_{ij}}{3}\overline{u_k u_k} \right)$$ (18)

2. Interaction of mean strain and fluctuating velocities $(\Pi_{ij})_2$ which is also referred to as return-to-isotropy of production term[20]:

$$(\Pi_{ij})_2 = -c_2\left(P_{ij} - \frac{\delta_{ij}}{3}P_{kk} \right)$$ (19)

3. Both processes in (18) and (19) are influenced by the presence of the wall[18] which is manifested by damping of fluctuations normal to the wall and enhancing fluctuations parallel to the wall. The constitutive equations can be expressed as:

$$(\Pi_{ij})_{w1} = \frac{\rho c_1' \varepsilon}{k}[\overline{u_k u_m}n_k n_m \delta_{ij} - \tfrac{3}{2}\overline{u_k u_k}n_k n_j - \tfrac{3}{2}\overline{u_k u_j}n_k n_i]f$$ (20)

$$(\Pi_{ij})_{w2} = \rho c_2'[(\Pi_{km})_2 n_k n_m \delta_{ij} - \tfrac{3}{2}(\Pi_{ik})_2 n_k n_j - \tfrac{3}{2}(\Pi_{jk})_2 n_k n_i]f$$ (21)

where

$$f = \frac{c_\mu^{0.75}k^{1.5}}{\varepsilon \kappa \Delta \eta}$$ (22)

with $\Delta \eta$ being wall normal distance, f is the wall-distance function and may be related to Cartesian velocity-oriented components by:

$$f_x = n_1^2 f; \qquad f_y = n_2^2 f; \qquad f_{xy} = n_1 n_2 f$$ (23)

The contribution of the turbulent diffusion can be approximated by:

$$D_{ij} = \left[c_\mu \frac{k^2}{\varepsilon}(\overline{u_i u_j})_{,k} \right]_{,k}$$ (24)

The transport equation (12) for Reynolds stresses is discretized in the same way as for any other dependent variable Φ.

The turbulence energy k and its rate of dissipation ε are calculated by:

$$\frac{\partial}{\partial x_i}(\rho U_i k) = \frac{\partial}{\partial x_i}\left[\left(\mu + \frac{\mu_t}{\sigma_k}\right)\frac{\partial k}{\partial x_i}\right] - \rho\varepsilon + Prod. \tag{25}$$

$$\frac{\partial}{\partial x_i}(\rho U_i \varepsilon) = \frac{\partial}{\partial x_i}\left[\left(\mu + \frac{\mu_t}{\sigma_\varepsilon}\right)\frac{\partial \varepsilon}{\partial x_i}\right] + \frac{\varepsilon}{k}(c_{\varepsilon1} Prod. - c_{\varepsilon2}\rho\varepsilon) \tag{26}$$

where the production term, *Prod.*, have the following form in the Reynolds stress modelling (*RSM*):

$$Prod. \equiv P_{ij} = -\rho\overline{u_i u_k}\frac{\partial U_j}{\partial x_k} - \rho\overline{u_j u_k}\frac{\partial U_i}{\partial x_k} \tag{27}$$

whereas in the $k-\varepsilon$ model:

$$Prod. \equiv P_k = \mu_t\left(\frac{\partial U_i}{\partial x_j} + \frac{\partial U_j}{\partial x_i}\right)\frac{\partial U_i}{\partial x_j} \tag{28}$$

BOUNDARY CONDITION

Inlet and outlet

At the inlet and outlet of the module, conditions of periodicity are imposed, i.e.

$$\Phi(x, y) = \Phi(x + L, y) \qquad \Phi = U, V, P^*, \Theta, k, \varepsilon, \overline{u_i u_j}, \lambda$$

Momentum equations

Due to the viscous influences near walls, the local Reynolds number becomes very small and thus the turbulence model which is designed for high Reynolds number becomes inadequate. Both this fact and the steep variation of properties near the walls necessitate special treatment for nodes close to the wall.

In the following explanation of the treatment of turbulence quantities near the wall, it is assumed that the region near the wall consists of two layers. The layer nearest the wall is designated the 'viscous sublayer' in which the turbulent viscosity is much smaller than the molecular viscosity, i.e. the turbulent shear stress is negligible. Ignoring the buffer layer, the second layer is designated the 'inertial sublayer' in which the turbulent viscosity is much greater than molecular viscosity, making it a fully turbulent region. These two layers are the wall dominated regions and it is assumed that the total shear stress is constant. The point $y^+ = 11.63$ is defined to dispose the buffer (transition) layer, and it corresponds to the intersection point between the log-law and the near-wall linear law. Above this point the flow is assumed purely turbulent and below this point the flow is assumed purely viscous.

Since the streamwise pressure gradient is assumed to be negligible, the momentum equation reduces to a particularly simple one-dimensional form:

$$\tau = (\mu + \mu_t)\frac{\partial U}{\partial y} \tag{29}$$

The wall function implemented in the calculation procedure can be summarized as follows:

(a) if $y^+ \geqslant 11.63$ where $\mu_t/\mu \gg 1$, $\tau \simeq \tau_w$

1. The wall shear stress is obtained by calculating the turbulent viscosity at the node adjacent to the wall from the log-law[21]. The turbulent viscosity used in the momentum equations is prescribed at the nodes adjacent to the wall (index P) as follows:

$$\tau_w = \rho U_*^2 = \mu_t \frac{\partial U}{\partial \eta} \approx \mu_t \frac{U}{\eta} \tag{30}$$

For μ_t we obtain:

$$\mu_t = \frac{U_*}{U} \rho U_* \eta \tag{31}$$

The law of the wall can be written:

$$\frac{U}{U_*} = \frac{1}{k} \ln(E\eta^+) \tag{32}$$

Finally, we have for μ_t:

$$\mu_t = \frac{\rho U_* \eta \kappa}{\ln(E\eta^+)} \tag{33}$$

where $E = 9$ and the von Karman constant, $\kappa = 0.41$. η denotes the normal distance to the wall.
2. The turbulent kinetic energy is set as:

$$k = c_\mu^{-0.5} U_*^2 \tag{34}$$

3. The turbulent kinetic energy dissipation rate is set as:

$$\varepsilon = \frac{U_*^3}{\kappa y} \tag{35}$$

4. The shear stress is obtained by:

$$\tau_w = \rho U_*^2 \tag{36}$$

(b) if $y^+ \leqslant 11.63$ where $\mu_t/\mu \ll 1$, $\tau \simeq \tau_w$

1. U_* is calculated by:

$$U_* = \sqrt{\frac{U_P \nu}{\eta}} \tag{37}$$

2. The procedure 2–4, as explained above, is followed.

Temperature equation

A treatment similar to that of the momentum equations is applied to the temperature equation. The transport equation at the wall reduces to:

$$q = (\Gamma + \Gamma_t) c_p \frac{\partial T}{\partial y} \tag{38}$$

It should be mentioned that the heat flux across the viscous sub-layer is assumed to be constant. As in the momentum transport treatment, the point $y^+ = 11.63$ is also defined here for disposing the buffer layer. If $y^+ \leqslant 11.63$ the transport is assumed to be due to only molecular activity, and the expression for the heat flux parameter T^+ is a simple one.

If $y^+ \geqslant 11.63$, the transport is assumed to be entirely due to turbulence. The heat flux parameter T^+ becomes a logarithmic function of y^+.

The solution procedure used is summarized as follows:

(a) if $y^+ \geqslant 11.63$ where $\Gamma_t/\Gamma \gg 1$, $q \simeq q_w$

q_w is calculated by using the following relation:

$$T^+ = \frac{(T_w - T_P)\rho c_p U_*}{q_w} = \sigma_t \left[U^+ + P\left(\frac{Pr}{\sigma_t}\right) \right] \tag{39}$$

from which it follows:

$$\frac{q_w}{c_p} = \frac{\rho U_*(T_w - T_p)}{\sigma_t \left[U^+ + P\left(\frac{Pr}{\sigma_t}\right) \right]} \tag{40}$$

where, according to Jayatillika[22], the P-function is defined as:

$$P\left(\frac{Pr}{\sigma_t}\right) = 9.24 \left[\left(\frac{Pr}{\sigma_t}\right)^{0.75} - 1 \right]\left[1 + 0.28e^{(-0.007/(Pr/\sigma_t))}\right] \tag{41}$$

(b) If $y^+ \leqslant 11.63$ where $\Gamma_t/\Gamma \ll 1$, $q \simeq q_w$

q_w is calculated by using the following relation

$$T^+ = \frac{\rho U_* y}{\dfrac{\mu}{Pr}} = \frac{(T_w - T_p)\rho c_p U^*}{q_w} \tag{42}$$

from which it follows:

$$\frac{q_w}{c_p} = \frac{\mu}{Pr\,y}(T_w - T_p) \tag{43}$$

Reynolds stress transport equations

The boundary condition of the stresses are obtained by the method presented by Lein and Leschziner[23]. The values of the stresses in the log-law region are computed by applying the stress equation to local energy equilibrium, and setting the wall distance function equal to unity and using $\varepsilon = U_*^3/\kappa\Delta\eta$. We then have:

$$\widehat{u^2} = 1.098k \tag{44}$$

$$\widehat{v^2} = 0.247k \tag{45}$$

$$\widehat{uv} = 0.255k \tag{46}$$

The above stresses are wall-oriented and should be transformed to the Cartesian coordinate system in which the velocity components are prescribed within the numerical scheme.

$$\overline{u^2} = \widehat{u^2}t_1^2 + \widehat{v^2}n_1^2 + 2\widehat{uv}t_1n_1 \tag{47}$$

$$\overline{v^2} = \widehat{u^2}t_2^2 + \widehat{v^2}n_2^2 + 2\widehat{uv}t_2n_2 \tag{48}$$

$$\overline{uv} = \widehat{u^2}t_1t_2 + \widehat{v^2}n_1n_2 + \widehat{uv}(t_1n_2 + t_2n_1) \tag{49}$$

where t_1, t_2, n_1 and n_2 are the tangential and normal components of the wall-oriented unit vector, respectively.

NUMERICAL SOLUTION PROCEDURE

To deal with complex geometries, a boundary fitted coordinate method is used. In principle, the complex flow domain in the physical space is mapped into a rectangular domain in the computational space by using a curvilinear coordinate transformation. This means that the Cartesian coordinate system x_i in the physical domain is replaced by a general non-orthogonal coordinate system ξ_i.

The momentum equations are solved for the velocity components U and V in the fixed Cartesian directions on a non-staggered grid. All the variables are thus stored at the centre of the control volume. In order to avoid non-physical oscillations in pressure and velocity, the Rhie–Chow interpolation method is used to compute the velocity components at the control volume faces. The pressure–velocity coupling is handled by the SIMPLEC method and the convective terms are treated by the hybrid scheme. TDMA-based algorithms are applied for solving the algebraic equations. Further details are provided in References 24 and 25.

REYNOLDS NUMBER

The Reynolds number is calculated as:

$$Re = \frac{U_m 2H}{\nu} = \frac{2\dot{m}}{\mu} \tag{50}$$

where ν is the kinematic viscosity and μ the dynamic viscosity. The mass flow rate $\dot{m}$ through a module is evaluated by:

$$\dot{m} = \rho \int_0^H U \, dy \tag{51}$$

The velocity U depends on the non-periodic pressure gradient β and therefore, (50) and (51) provide a relation between the Re and β.

PRESSURE DROP

The per-cycle pressure drop Δp is calculated as:

$$\Delta p = \beta L \tag{52}$$

It is desirable to compare this pressure drop with the corresponding value for a straight parallel plate duct with hydraulic diameter $(D_h = 2H)$. From any standard textbook on fluid mechanics, e.g. Özisik[26], the pressure drop Δp (fully developed flow) in a straight parallel plate duct can

be found to be:

$$\Delta p_0 = f_f \frac{L}{2H} \frac{\rho U_m^2}{2} \tag{53}$$

where subscript (o) refers to the straight parallel plate duct. The friction factor f_f is calculated by the Prandtl friction law[24]:

$$\frac{1}{\sqrt{f_f}} = 2 \log(Re\sqrt{f_f}) - 0.8 \tag{54}$$

For identical mass flows, the Reynolds number of the straight parallel plate duct becomes equal to that of the corrugated duct and the ratio of the per-cycle pressure drops can be expressed as:

$$\frac{\left(\dfrac{\Delta p}{L}\right)}{\left(\dfrac{\Delta p}{L}\right)_0} = \frac{4H\beta}{\rho f_f U_m^2} \tag{55}$$

where U_m is the mean velocity.

LOCAL NUSSELT NUMBER

By using the conventional definition of the heat transfer coefficient between the wall and the fluid[26] we obtain:

$$Nu_x = \frac{hD_h}{k_c} = \frac{q_w 2H}{k_c(T_w - T_b)} \tag{56}$$

where Nu_x is the local Nusselt number, k_c the thermal conductivity of the fluid and q_w the heat flux to the wall.

The universal temperature profile is used to calculate the heat transfer to the wall of the duct. With the dimensionless height of the duct $H^+ = U_* H/\nu$ and with the dimensionless bulk temperature defined as:

$$T_b^+ = \frac{(T_w - T_b)\rho c_p U_*}{q_w} \tag{57}$$

the local Nusselt number can be written as:

$$Nu_x = 2Pr \frac{H^+}{T_b^+} \tag{58}$$

The bulk temperature is defined by:

$$T_w - T_b = \frac{\int_0^H |U|(T_w - T)\,dy}{\int_0^H |U|\,dy} \tag{59}$$

Introducing the dimensionless variables, we obtain:

$$T_b^+ = \frac{\int_0^{H^+} |U^+|T^+\,dy^+}{\int_0^{H^+} |U^+|\,dy^+} \tag{60}$$

where U^+ and T^+ are as defined previously.

OVERALL NUSSELT NUMBER

The overall heat transfer coefficient h_{av} is defined by an overall heat balance, that is:

$$h_{av} = \frac{\dot{Q}}{A \Delta T_{wb}} \tag{61}$$

The average wall-to-bulk temperature difference is evaluated as:

$$\Delta T_{wb} = \tfrac{1}{2}\{(T_w - T_{b2}) + (T_w - T_{b1})\} \tag{62}$$

and the total heat flux $\dot{Q}$ is given by:

$$\dot{Q} = \dot{m}c_p(T_{b2} - T_{b1}) \tag{63}$$

where $\dot{m}$ is the mass flow rate and c_p is the specific heat of the fluid. Combining (61), (62), (63) and the definition of the Nusselt number we have:

$$Nu = \frac{(1 - \gamma)H}{(1 + \gamma)A} PrRe \tag{64}$$

where γ is defined as:

$$\gamma = \frac{(T_w - T_{b2})}{(T_w - T_{b1})} \tag{65}$$

The quantity γ is obtained by integrating (7) along the cycle length.

SAMPLE CALCULATIONS

The Prandtl number was set equal to 0.72 and Reynolds number was varied from 3000 to 35,000 by choosing appropriate values of the per-cycle pressure gradient, β.

Convergence

The computations were terminated when the sum of absolute residuals normalized by the inflow fluxes was below 10^{-4} for all the variables. To achieve convergence in the solution, under-relaxation factors of 0.7, 0.4 and 0.5 were chosen for the velocities, pressure correction and turbulent quantities, respectively. About 1000 to 4000 iterations, depending on the Reynolds number, geometrical parameters, and the turbulence model were required to obtain a converged solution for the velocity field. The temperature field, which was also solved iteratively (under-relaxation factor 0.8), converged within a few hundred iterations if a known velocity field was used.

Grid size effects and numerical accuracy

The grid points are distributed in a uniform manner. Each control volume contains one node at its centre but the boundary adjacent volumes contain two nodes, one at the centre and one at the boundary. Exploratory test runs were carried out for several different grid sizes for the case of $\phi = 45°$ and $H/L = 1/5$. The velocity profiles for these grids at the second corner BB (*Figure 1*) are plotted in *Figure 2*. The maximum changes in the velocity between the most coarse mesh (83 × 24) and the finest mesh (111 × 34) are within 7%. A (100 × 34) mesh was chosen in the final calculations to maintain a reasonable accuracy and relatively moderate computing costs.

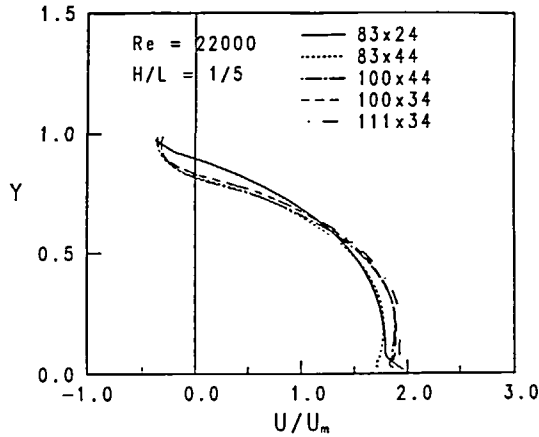All calculations were carried out on a DEC 3100 work-station.

Figure 2 Streamwise velocity profiles in the channel computed by RSM for different mesh sizes

Comparison with previous results

The comparison of the overall Nusselt number with the experimental data of O'Brien and Sparrow[1] in a corrugated duct with a corrugation angle of 30° and a bend angle of 120° is given in *Figure 3a*. As seen from this Figure, the results of the present computations with employment of the Reynolds stress closure agree well with the experimental data. The overall Nusselt numbers obtained by using the $k-\varepsilon$ model show a 38% overprediction compared with the second moment closure.
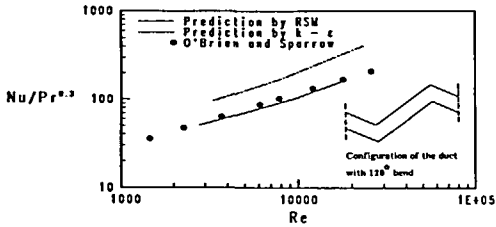
Figure 3a Comparison of the average Nusselt number for computational and experimental results
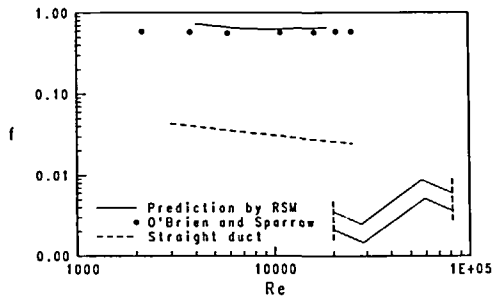
Figure 3b Comparison of the average friction coefficient for computational and experimental results
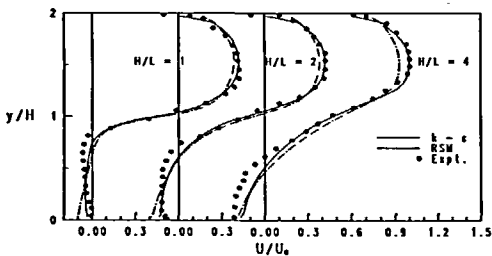
Figure 3c Velocity profiles in a backward-facing step flow
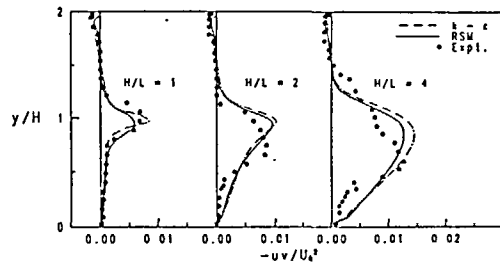
Figure 3d Reynolds shear stress profiles in a backward-facing step flow

Figure 3b presents the comparison of the computed friction factor f_f with the experimental data. The agreement is reasonably good. The difference between the calculated friction factor by using the $k-\varepsilon$ model and the RSM model is very small and for this reason only the calculated results by RSM is shown in *Figure 3b*.

Additional confidence was gained by computing the fluid flow in a backward-facing step. The computed results of the velocity and the Reynolds shear stress distribution in the region behind the step were compared with the experimental data of Durst and Schmitt[27], see *Figures 3c* and *3d*. In both the recirculating and recovering regions, agreement between the present computations and the experimental data are reasonably good.

RESULTS AND DISCUSSION

Overall Nusselt number and pressure drop

The overall Nusselt numbers are displayed on log–log coordinates in *Figures 4* and *5*. In these Figures $Nu/Pr^{0.3}$ is plotted as a function of Reynolds number for two corrugation angles and two H/L ratios. The computations by the second-moment closure (RSM) model and the $k-\varepsilon$ model are presented. It is noteworthy that the $k-\varepsilon$ predictions are 25% higher than those of the RSM except in the case of $\phi = 15$ and $H/L = 1/3$.

The reason for higher prediction by the $k-\varepsilon$ can be explained by the help of *Figures 6* and *7*. Two distinct differences can be observed in these Figures, i.e. the difference in velocity profiles and recirculation zones. RSM predicts much steeper velocity gradients which in turn cause lower velocities close to the wall and therefore lower convection to the wall. Since the recirculation predicted by RSM is larger than that of the $k-\varepsilon$ prediction, the re-attachment takes place further downstream.

Results of the pressure drop ratios are plotted in *Figure 8*. In the ducts with a corrugation angle 45° the pressure drop increases as Reynolds number increases. However, this is not true in the ducts with corrugation angle 15°. As the Reynolds number increases the pressure drop ratios decrease moderately and become almost constant at high Reynolds numbers.

Local Nusselt number

The distribution of the local Nusselt numbers along the duct length are presented in *Figure 9*. In *Figure 9a* the local Nusselt numbers for $\phi = 45°$ and $H/L = 1/5$ for three different Reynolds numbers are displayed. In *Figure 9b* Nu_x is presented for $\phi = 45°$ and two different H/L. The difference in the Nu_x prediction by the RSM and $k-\varepsilon$ models are presented in *Figure 9c*. These Figures should be studied in conjunction with the figures displaying the velocity profiles. For
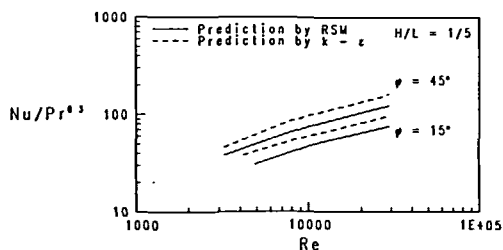

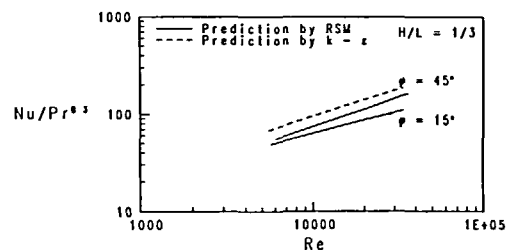*Figure 4* Average Nusselt number as a function of Reynolds number for $H/L = 1/5$, and $\phi = 45°$ and 15°

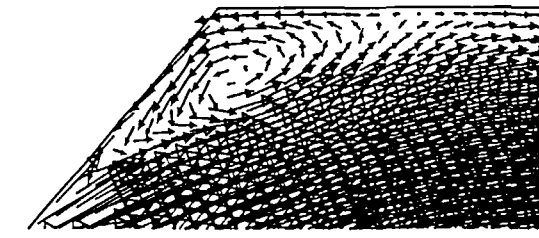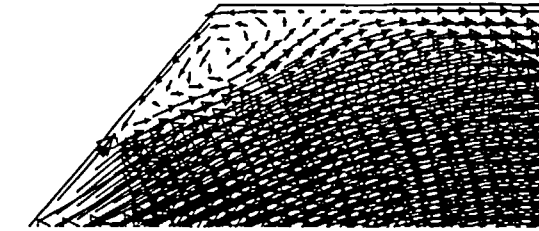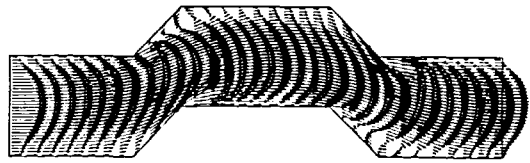*Figure 5* Average Nusselt number as a function of Reynolds number for $H/L = 1/3$, and $\phi = 45°$ and 15°

Prediction by RSM - model

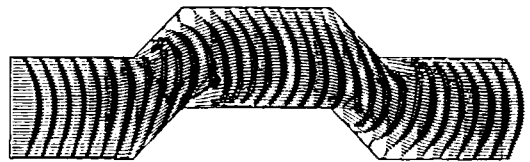Prediction by k - ε - model

Figure 6 Velocity vectors at the upper upstream corner in the duct with $H/L = 1/5$, $\phi = 45°$ and $Re = 26,700$

Prediction by RSM - model

Prediction by k - ε - model

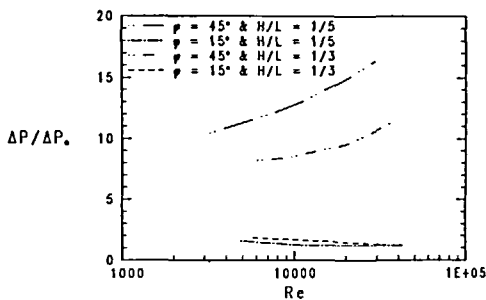**Figure 7** Velocity vectors in the duct with $H/L = 1/5$, $\phi = 45°$ and $Re = 26,700$

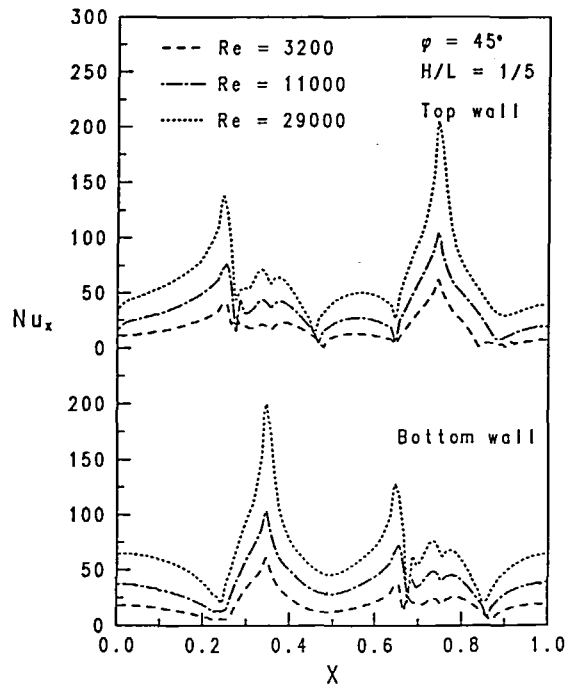**Figure 8** Pressure drop ratios as a function of Reynolds number

Figure 9a Local Nusselt number distribution for three different Reynolds numbers and $\phi = 45°$ and $H/L = 1/5$
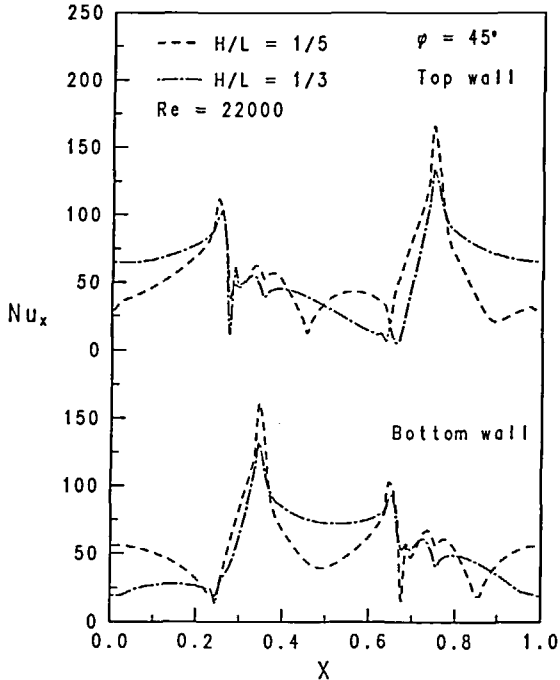
Figure 9b Local Nusselt number distribution for two different module aspect ratios and $\phi = 45°$ and $Re = 22,000$
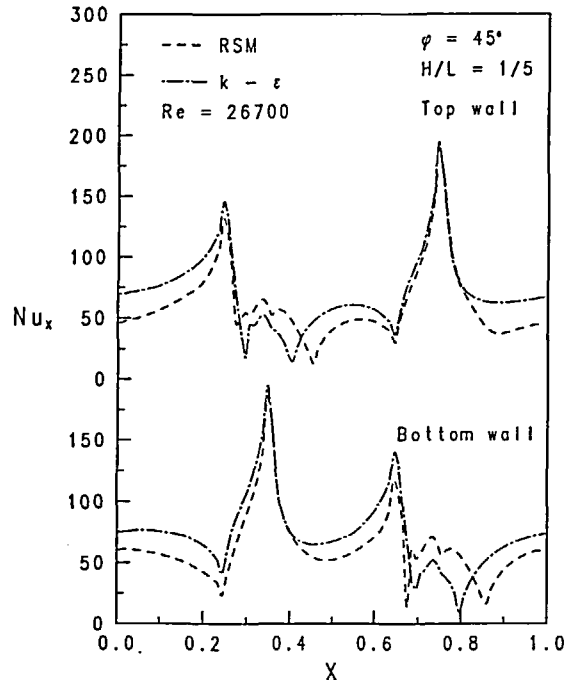
Figure 9c Comparison of local Nusselt number distribution computed by $k-\varepsilon$ and RSM turbulence models

convenience the duct is divided to five different sections. The positions of these sections are shown in *Figure 1*.

At the top wall of the first section, Nu_x distribution shows a slight increase at the beginning of the section and a sharp increase to a maximum at the end of the section. At the bottom wall unlike the top wall Nu_x decreases. At the interface of the sections one and two, Nu_x decreases sharply to a minimum at the top wall and a sharp increase appears at the bottom wall. However, an interesting phenomena can be observed at the upper oblique wall in the second section. At this wall, Nu_x forms a triple peak pattern. This phenomena can be described by means of *Figure 10*. As the Re increases the recirculation zone becomes smaller and its centre moves closer to the corner and the intensity of the recirculation increases. At point d_1 at the interface corner the Nu_x starts to decrease due to the deflected velocity which causes no convention to the wall, see *Figures 7* and *11*. Between point d_1 and d_2 where the upgoing flow meets the down coming flow, Nu_x continues to decline. At this distance, the velocity vectors run almost parallel with the oblique wall. At point d_2 the first peak takes place. From point d_2 to d_3 the velocity vectors are no longer parallel to the wall and the impingement of the velocity vectors at the wall can be observed. This causes higher convection to the wall and therefore the heat transfer increases at the wall. The impingement at the end of the oblique wall is higher, see *Figure 6*, which causes the second peak. Due to the curved nature of the flow path in the recirculation the convection to the wall at the corner reduces and therefore the local Nusselt number right at the corner decreases (see *Figure 6*). However, at the beginning of the third section and before the corner the convection to the wall is higher than the convection at the corner. This causes the appearance of the third peak. It is worthwhile to note that the recirculation acts as a conveyor carrying
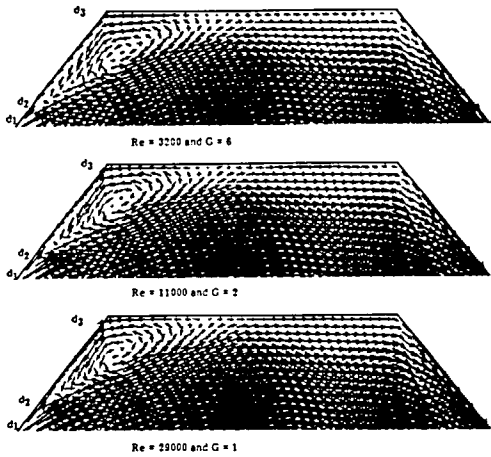
Figure 10 Velocity vectors at the upper upstream corner in the duct with $H/L = 1/5$, $\phi = 45°$ at three different Reynolds numbers

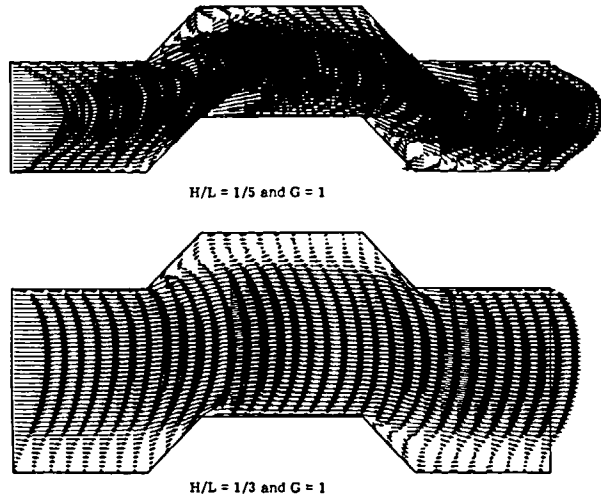*Figure 11* Velocity vectors in the duct with $\phi = 45°$ and $Re = 22,000$ at two different module aspect ratios

heat between the shear layer and the wall. At the upper wall of the third section the Nu_x decreases upto the re-attachment point and increases moderately thereafter. However, as at the upper corner at the beginning of this section Nu_x decreases. At the bottom wall, due to very high convection to the oblique wall Nu_x increases sharply. Nu_x falls sharply at the beginning of the third section on the bottom wall and increases as convection to the wall increases (see *Figure 7*). The distribution of the local Nusselt number at the bottom and top walls of the fourth section is similar to that of the top and bottom walls of the second section, respectively. Nu_x distributions in the fifth and first sections are similar but the mirror image of each other.

By increasing H/L, the recirculation zones are stretched along the wall (see *Figure 11*) causing lower convection to the wall at the top of section three and bottom walls of sections one and five. Thus Nu_x distribution in the duct with $H/L = 1/3$ is lower in these parts. Due to the longer recirculation zone and according to the continuity, the fluid flow at the top wall of sections one and five, and the bottom wall of section three is larger than in the case of the duct with $H/L = 1/5$ (see *Figure 11*). Therefore, higher heat transfer is achieved in these regions. At the downstream part of the bottom and top oblique walls of the second and fourth sections, respectively, the higher forced convection causes higher local Nusselt number distribution.

At this point it is worthwhile to mention that due to the complex flow situation the use of wall functions in the separated flow regions may not be so accurate. However, other procedures are scarce and those available are not necessarily more accurate or physically correct.

In *Figure 9c* comparison between the RSM prediction and $k-\varepsilon$ prediction of Nu_x is presented. At both the top and bottom walls $k-\varepsilon$ predicts higher heat transfer. This is due to the prediction of higher velocities by $k-\varepsilon$ near the wall region.

CONCLUSION

A numerical model is developed to investigate the fully developed heat transfer and fluid flow characteristics for turbulent flow through streamwise-periodic corrugated ducts with two different

corrugation angles and two different duct height to duct length ratios. The governing equations are solved by a body-fitted finite-volume method for elliptic flow in complex geometries using collocated variables. Two different turbulence models are used to approximate the Reynolds stresses. A global new method for treatment of the boundary conditions in curvilinear boundaries are presented. The results were obtained for a uniform wall temperature for Reynolds number ranging from around 3000 to 35,000. Comparison with experimental data approves that the $k-\varepsilon$ model overpredicts the Nusselt numbers. The plot of the velocity vectors show a complex flow pattern. The effects of the separation, deflection, recirculation and re-attachment on the heat transfer mechanisms are described in details. The overall Nusselt number and pressure drop are increased by increasing Reynolds number. The results indicate that the optimum duct geometries at higher Reynolds number might be found in ducts with lower corrugation angles at which the Nusselt number is relatively high while the pressure drop is relatively low compared with ducts with higher corrugation angles.

ACKNOWLEDGEMENT

REFERENCES

1 O'Brien, J. E. and Sparrow, E. M. Corrugated-duct heat transfer, pressure drop, and flow visualization, *J. Heat Transfer*, **104**, 410–416 (1982)
2 Izumi, R., Yamashita, H., Kaga, S. and Miyajima, N. Fluid flow and heat transfer in corrugated wall channels—experimental study for many bends, *Proc. 19th JSME Symp. Heat Transfer*, Paper No. A101 (1982)
3 Goldstein, L. and Sparrow, E. M. Heat/mass transfer characteristics for flow in corrugated wall channel, *J. Heat Transfer*, **99**, 187–195 (1977)
4 Farhanieh, B. and Sunden, B. Fully developed laminar fluid flow and heat transfer in streamwise-periodic corrugated ducts with constant cross-sectional area, *Int. J. Num. Meth. Heat Fluid Flow*, **2**, 379–390 (1992)
5 Amano, R. S., Bagherlee, A., Smith, R. J. and Niess, T. G. Turbulent heat transfer in corrugated-wall channels with and without fins, *J. Heat Transfer*, **109**, 62–109 (1987)
6 Fass, S. E. and McEligot, D. M. Convective heat transfer for ship propulsion, *Report No. 1248-7, ONR*, Aerospace and Mechanical Engineering Department, University of Arizona (1980)
7 Webb, R. L. Enhancement of single phase heat transfer, in *Handbook of Single-Phase Convective Heat Transfer*, (S. Kakac, R. K. Shah and W. Aung), Wiley–Interscience, New York (1987)
8 Patankar, S. V., Liu, C. H. and Sparrow, E. M. Fully developed flow and heat transfer in ducts having streamwise-periodic variations of cross-sectional area, *J. Heat Transfer*, **99**, 180–186 (1977)
9 Sparrow, E. M. and Prata, A. T. Numerical solution for laminar flow and heat transfer in a periodically converging–diverging tube with experimental confirmation, *Num. Heat Transfer*, **6**, 441–461 (1983)
10 Prata, A. T. and Sparrow, E. M. Heat transfer and fluid flow characteristics for an annulus of periodically varying cross-section, *Num. Heat Transfer*, **7**, 285–304 (1984)
11 Rowley, G. L. and Patankar, S. V. Analysis of laminar flow and heat transfer in tubes with internal circumferential fins, *Int. J. Heat Mass Transfer*, **27**, 553–560 (1984)
12 Faghri, M. and Asako, Y. Numerical determination of heat transfer and pressure drop characteristics for converging–diverging flow channel, *ASME Winter A. Meet.*, Paper no. 84-WA-HT-12 (1984)
13 Asako, Y. and Faghri, M. Heat transfer and fluid flow analysis for an array of interrupted plates, positioned obliquely to the flow direction, *Proc. 8th Int. Heat Transfer Conf.*, **2**, 421–427 (1986)
14 Webb, B. W. and Ramadhyani, S. Conjugate heat transfer in a channel with staggered ribs, *Int. J. Heat Mass Transfer*, **28**, 1679–1687 (1985)
15 Sunden, B. and Trollheden, S. Periodic laminar flow and heat transfer in a corrugated two-dimensional channel, *Int. Commun. Heat Mass Transfer*, **16**, 215–225 (1989)
16 Farhanieh, B. and Sunden, B. Numerical investigation of periodic laminar heat transfer and fluid flow characteristics in parallel plate ducts with streamwise-periodic cavities, *Int. J. Num. Meth. Heat Fluid Flow*, **1**, 143–157 (1991)
17 Jones, W. P. and Launder, B. E. The prediction of laminarization with a two-equation model of turbulence, *Int. J. Heat Mass Transfer*, **15**, 301–314 (1972)
18 Gibson, M. M. and Launder, B. E. Ground effects on pressure fluctuations in the atmospheric boundary layer, *J. Fluid Mech.*, **86**, 491 (1978)

19 Rotta, J. C. *Turbulente Strömungen*, B. G. Teubner, Stuttgart (1972)
20 Naot, D., Shavit, A. and Wolfshtein, M. Interaction between components of the turbulent velocity correlation tensor, *Israel J. Technol.*, 8, 259 (1970)
21 Farhanieh, B., Davidson, L. and Sunden, B. Employment of second order closure for calculation of turbulent recirculating flows in complex geometrics with collocated variable arrangement, *Int. J. Num. Meth. Fluids*, in press (1993)
22 Jayatillaka, C. L. V. *Progr. Heat Mass Transfer*, 1, 193 (1969)
23 Lein, F. S. and Leschziner, M. A. Second-moment modeling of recirculating flow with a non-orthogonal collocated finite-volume algorithm, *8th Symp. Turbulent Shear Flows, Munich* (1991)
24 Davidson, L. and Farhanieh, B. CALC–BFC: a finite-volume code employing collocated variable arrangement and cartesian velocity components for computation of heat and mass transfer in complex three-dimensional geometries, *Publication No. 91/14*, Dept. of Thermo- and Fluid Dynamics, Chalmers University of Technology, Göteborg, Sweden (1991)
25 Farhanieh, B. and Sundén, B. Three dimensional laminar flow and heat transfer in entrance region of trapezoidal ducts, *Int. J. Num. Meth. Fluids*, 13, 537–556 (1991)
26 Özisik, M. N. *Basic Heat Transfer*, McGraw-Hill, Tokyo (1977)
27 Durst, F. and Schmitt, F. Experimental studies of high Reynolds number backward-facing step flows, *Proc. 5th Symp. Turbulent Shear Flows, Cornell Univ.*, (1985)